

Main Manuscript for

Motion and Trapping of Micro- and Millimeter Spheroid Particles on the Air-Paramagnetic Liquid Interface

Zoran Cenev¹, Alois Würger^{2*} and Quan Zhou^{1*}

¹Department of Electrical Engineering and Automation, School of Electrical Engineering, Aalto University, Maarintie 8, FI-00076 Espoo, Finland

²Laboratoire Ondes et Matière d'Aquitaine, Université de Bordeaux and CNRS, 33405 Talence, France

* Alois Würger and Quan Zhou

Email: zoran.cenev@aalto.fi, alois.wurger@u-bordeaux.fr and quan.zhou@aalto.fi

<https://orcid.org/0000-0001-7434-3880>

<https://orcid.org/0000-0003-1499-1960>

<https://orcid.org/0000-0002-3819-3878>

Classification

Physical sciences. Applied Physical Sciences.

Keywords

paramagnetic liquid; interface; motion; particles; inverse Moses effect;

Author Contributions

Z.C. observed the pulling and the trapping motion. Z.C. and Q.Z. conceived the research, designed the experiments, analyzed the data and postulated the initial theoretical explanation. Z.C. built the experimental setup and performed the experiments. A.W. constructed the theoretical model. Z.C. implemented the theoretical model and generated the numerical results. Q.Z. supervised the research. All authors wrote the paper. Data and materials availability from authors.

This PDF file includes:

Main Text

Figures 1 to 5

Abstract

The motion of matter on air-liquid interface is of great importance in biology, physics, chemistry and engineering. Here we study non-magnetic and magnetic spheroid particles floating on the surface of a paramagnetic liquid and actuated by a contact-free magnet. The approaching magnet deforms the paramagnetic liquid interface and results in a rich dynamical behavior of the particle. Depending on geometry and on material parameters, the particle may be trapped at the center of the deformation profile, being pushed away from the magnet, or be trapped at an off-center position. The underlying physical mechanism is theorized as an interplay of the curvature of the interface deformation created by the non-uniform magnetic field from the magnet, the gravitational potential and the magnetic energy from the particle and the liquid. For highly concentrated paramagnetic liquids the magnetic buoyancy has a dominant role in the total energy of a floating particle on an air-paramagnetic liquid interface. Additionally, the discovered phenomenon has been demonstrated in directed self-assembly and robotic particle guiding.

Significance Statement

Understanding the motion of particles on an air-liquid interface can impact a wide range of scientific fields and applications. Controlling the motion of particles using magnetic fields has also attracted great attention recently. However, the current understanding of the motion of non-magnetic particles on air-paramagnetic liquid interface subjected to a magnetic field is insufficient, consequently hindering its potential application. Here we report the trapping behavior and underlying mechanism of non-magnetic and magnetic light-weighted particles on the air-paramagnetic liquid interface when the interface is deformed by a non-uniform magnetic field. Additionally, we show the first demonstrations of the new motion phenomena in directed self-assembly and robotic particle guiding.

Main Text

Introduction

The motion of organisms on an air-liquid interface is a fundamental phenomenon in nature (1), has been profoundly studied (2), and extended to manipulate artificial objects (3). The motion of small objects at air-liquid interfaces can be induced by surface tension gradients (4, 5), magnetic fields (6–9), or perturbed interfaces from mechanical (10, 11) or field stimuli (12–16). Early work has shown that non-magnetic spherical particles on the air-paramagnetic liquid interface can be pushed away from a magnet (17, 18), attributed to negative magnetophoresis (19). Recently, pushing non-magnetic liquid droplets and liquid marbles away from the magnet on an air-paramagnetic liquid interface has been also demonstrated (20). The motion of the droplets and the liquid marbles was attributed to the surface deformation of the paramagnetic liquid caused by the magnet, a phenomenon known as the inverse Moses effect (21). These previous works have shown only pushing motion of the objects floating on the air-paramagnetic liquid interface. However, such a prevalent notion is not complete.

In this paper, we show that non-magnetic spheroid particles on an air-paramagnetic liquid interface besides being pushed can also be pulled towards the magnet and eventually trapped at a finite distance from the centerline of the magnet. We argue that the motion mechanism is novel, and it represents an interplay of the curvature of the meniscus created by the magnet, the gravitational, and the magnetic potential of the particle and the liquid. We demonstrate for the first time that for highly concentrated paramagnetic liquids the magnetic buoyancy has a dominant role in the total energy. Additionally, when the non-magnetic spheroid particles are substituted with magnetic

particles, the trapping point shifts to the peak of interface deformation induced by the magnet on the surface of the paramagnetic liquid.

We use cylindrical rare earth permanent magnet (25 mm × ϕ 5 mm) to induce deformation on the air-paramagnetic liquid interface without contacting the paramagnetic liquid. Particles floating on the interface then move towards the locations with minimum energy, which can be away from, at the base or at the peak of the deformed interface depending on the effective mass and the magnetic susceptibility of the particle. We have derived a model formulating the interface deformation of a paramagnetic liquid under nonlinear magnetic field, and quantitatively analyzed the motion of the particles induced by the deformed interface theoretically and experimentally. Additionally, we have applied the newly discovered pulling and trapping motion phenomenon of floating non-magnetic EPS particles in directed self-assembly and robotic particle guiding on the surface of a magnetic medium.

Results and Discussion

Experimental observation of displacement modes on particles on air-paramagnetic liquid interface.

In our studies, two types of paramagnetic liquids were used: holmium-based and manganese dichloride-based aqueous solution (see Table S1). Additionally, four types of spheroid particles were used: polystyrene (PS) and polyethylene (PE) particles as a type of higher-density particles with negligible magnetic susceptibility, expanded polystyrene (EPS) particles as a type of lower-density particles with negligible magnetic susceptibility; and hollow ceramic (HC) particles as a type of lower-density particles and magnetic susceptibility higher than the paramagnetic liquids (see Table S2).

Figure 1 shows the different motion modes of the particles residing on the deformed air-paramagnetic liquid interface. PS and PE particles are repelled, i.e. pushed away from the magnet (Figure 1a-c) on both paramagnetic liquids (Video S1). This repelling motion is in agreement with the earlier observations (17, 18). However, the EPS particles are pulled or pushed by the magnet depending on their initial locations, and finally trapped at the base of the deformed interface, Figure 1d-f. One should note that this is an axisymmetric case and therefore the off-center trapping location has a ring-shape potential well where these particles move towards. This motion has also been observed for both paramagnetic liquids (Video S2). For a HC particle, which is a magnetic particle, the motion is only towards the magnet with trapping location at the peak of the interface deformation (Figure 1g-i and Video S3). This motion was observed for both paramagnetic liquids as well. The experimental setup for conducting the experiments is illustrated in Figure S1a and detailed in the Materials and Methods section.

Effects from the air-paramagnetic liquid interface deformation

The relation between the vertical position of the magnet in respect to the height of the interface deformation and the trapping location of an EPS particle has been studied using a system illustrated in Figure 2a. The important parameters are the magnetic position h_M , the maximum interface deformation h_L , and the trapping location of an EPS particle, i.e. δ_{EPS} . Video S4 shows the experimental data. The experimental results for both paramagnetic liquids are shown in Figure 2b and c.

Both plots indicate negative correlations of the magnet position h_M in respect to the maximum interface deformation h_L , showing the closer the magnet to the paramagnetic liquid is, the greater the interface deformation becomes. The trapping location of an EPS particle δ_{EPS} is positively correlated with the magnet-to-paramagnetic liquid distance h_M , i.e. a smaller the magnet to the

paramagnetic liquid h_M leads to a closer trapping location to the centerline of the magnet δ_{EPS} , and vice versa.

Theoretical model

The behavior of a particle on the air-liquid interface is a process of minimizing the total energy E_{TOTAL} of the system, meaning the particle will always tend to go towards regions with minimum energy. The particle interacts with both, the deformation profile of the liquid interface, and with the magnetic field. Here we briefly discuss the contributions to the total energy

$$E_{TOTAL} = E_0 + E_G + E_I + E_M, \quad (1)$$

where $E_0 = \gamma\pi r_0^2(1 - |\cos \theta|)$ is a constant representing the adsorption energy at a flat horizontal interface, with surface tension of the paramagnetic liquid γ and a radius of the contact line $r_0 = a \sin \theta$ for liquid-sphere contact angle θ . With the effective mass m_{eff} , the gravitational acceleration g , and the profile of the interface deformation $u(\rho)$ as illustrated on Figure 2a, the potential energy reads as

$$E_G = m_{eff}gu(\rho). \quad (2)$$

where ρ denotes the radial distance from the centerline of the magnet. For a spherical particle of radius a floating on an air-paramagnetic liquid interface, neglecting the density of air, the effective mass is defined as:

$$m_{eff} = \rho_P V_P - \rho_L V_{imm} \quad (3)$$

where ρ_P and V_P are the density and the volume of the particle, ρ_L is the paramagnetic liquid density and the V_{imm} is the corresponding immersion volume:

$$V_{imm} = \left(\frac{\pi}{3}\right) a^3 (1 + 3c_0 - c_0^3) \quad (4)$$

with $c_0 = \cos \theta$ the degree of immersion (22–24) defined in terms of the cosine of the contact angle θ between the particle and the liquid. The experimentally measured contact angles of each particle with each paramagnetic liquid are given in Table S3 and the measurement protocol is explained in Materials and Methods section.

At a non-uniform interface the particle's capillary energy changes due to the superposition of the deformation profile $u(\rho)$ and the meniscus induced by the particle's effective weight gm_{eff} . With the capillary length $l = \sqrt{\gamma/g\rho_L}$ and the mean curvature of the deformed interface $H = \nabla^2 u$, the capillary energy is given by

$$E_I = m_{eff}gl^2H \quad (5)$$

The particle's magnetic energy has two contributions, which account for its own magnetization in the field B and for its magnetic buoyancy in the magnetic liquid. In the simplest case the susceptibilities are taken as constants, and we have

$$E_M = B^2 \frac{1}{\mu_0} (\chi_L V_{imm} - \chi_P V_P) \quad (6)$$

where μ_0 is the permeability of free space, and χ_L and χ_P are the magnetic susceptibilities of the paramagnetic liquid and the particle, respectively. The magnetic properties ($M_v H$ curves) from which the magnetic susceptibilities χ_L and χ_P can be derived are given in Figure S2. Finally, the total energy is an interplay among the deformation profile $u(\rho)$ and its curvature contribution $H(\rho)$ on one hand and the magnetic energy on the other. Therefore, we have:

$$E_{TOTAL} = E_0 + m_{eff} g (u(\rho) + l^2 H(\rho)) - (\chi_L V_{imm} - \chi_P V_P) B^2 \frac{1}{\mu_0}. \quad (7)$$

The linearized curvature of the meniscus $H(\rho)$ is given by the first and second derivatives of the interface deformation, $H(\rho) = u''(\rho) + u'(\rho)/\rho$. The axisymmetric representation of the shape of the meniscus $u(\rho)$ varies with the distance from the centerline, as shown in Figure 2a and it can be obtained by:

$$u(\rho) = \frac{1}{2\pi\gamma} \int_0^\infty dq q \int_0^{2\pi} d\phi K_0 \left(\frac{|\vec{\rho} - \vec{q}|}{l} \right) \Pi(q) \quad (8)$$

where $\vec{\rho}$ is the distance along the horizontal axis, \vec{q} is the sweeping vector, such that $|\vec{\rho} - \vec{q}| = \sqrt{\rho^2 + q^2 - 2\rho q \cos(\phi)}$, and ϕ the azimuthal angle between the two-dimensional vectors $\vec{\rho}$ and \vec{q} , K_0 is Bessel function of the second kind and $\Pi(q)$ is the Maxwell tensor at the interface plane $z = 0$. The maximum value for $u(\rho)$ is obtained at $u(\rho = 0)$, denoted by h_L and it is directly correlated by the magnet-to-liquid distance h_M as depicted in Figure 2. Detailed theoretical derivation of the energy profiles and the interface deformation are provided in the Supporting Information.

Comparison of experimental results and theoretical model

Figure 3a depicts the theoretically estimated interface deformation of a manganese dichloride-based paramagnetic liquid for five different magnet-to-liquid distances h_M , i.e. 2.3, 2.4, 2.5, 2.6 and 2.7 mm using the equation (8). The comparison of the maximum height of the meniscus h_L between theoretical estimations and experimental observations from Video S4 are shown in Figure 3b. For the mentioned vertical position of the magnet h_M of 2.3, 2.4, 2.5, 2.6 and 2.7 mm, the theoretically estimated values for h_L are 0.4, 0.37, 0.34, 0.31 and 0.28 mm and the observed values are 0.70, 0.52, 0.37, 0.24 and 0.09 mm, respectively. This discrepancy of ~40% can be attributed to the linearization of interface deformation u in terms of the Young-Laplace equation, the numerical error, and the measurement error. Additional influences may also be contributed by the change of local viscosity and/or surface tension (25) in the paramagnetic liquid in the presence of magnetic field. The estimated and observed interface deformations for the holmium-based paramagnetic liquid can be found in Figure S3.

The plots in Figure 4 a-d show the theoretically estimated individual energy contributions of PE, PS, HC and EPS particles, respectively. In these four plots, the gravitational energy is illustrated in blue, the capillary energy in green, the magnetic energy in red, and the sum of all these three energies in black color. The location of the minimum energy for the PE and the PS particles is further away from the interface deformation at distances greater than 10 mm where the precise location is not indicated. This estimation is in agreement with the observed behavior of the particles

in Video S1 and Figure 1 a-c. No trapping of particles has been theoretically estimated and neither observed, only pushing motion. Figure 4c shows the individual energy contributions for an HC particle. The magnetic energy dominates both the gravitational and the capillary contributions by about three orders of magnitude. The sum of the energies has a minimum at the distance $\rho = 0$, i.e. the peak of the deformed interface. This theoretical estimation agrees with the experimental observation in Figure 1g-i and Video S3. Figure 4d shows the energetic interplay for an EPS particle. If we ignore the local minimum from numerical error at the centerline of the magnet ($\rho = 0$), one can observe that the sum of the energy has a monolithically decreasing trend from $\rho = 0$ until $\rho \cong 7 \text{ mm}$. The capillary contribution E_I changes sign at $\rho \cong 4 \text{ mm}$ and reaches its minimum at $\rho \cong 6 \text{ mm}$. The gravitational energy has a monolithically increasing trend starting from $\sim -0.6 \times 10^{-8} \text{ J}$. The sum of the three energies creates a local minimum at $\rho \cong 7 \text{ mm}$. This local minimum represents the trapping location of the EPS particle. The plot in Figure 4d is calculated for magnet position $h_M = 2.3 \text{ mm}$.

Figure 4e shows the trapping locations for five magnet positions $h_M = 2.3, 2.4, 2.5, 2.6$ and 2.7 mm . Figure 4f compares the theoretically estimated local minima from Figure 4e with the experimentally observed trapping locations from Figure 2b. For the vertical position of the magnet h_M of 2.3, 2.4, 2.5, 2.6 and 2.7 mm, the theoretically estimated energy minima are 7.17, 7.29, 7.48, 7.63 and 7.79 mm and the observed trapping locations are 5.20, 5.40, 5.60, 5.80 and 6.00 mm, respectively. The discrepancy in the estimation location of minimum energy is $\sim 28\%$, which we attribute to the inaccuracy of the theoretical estimation of the deformed interface $u(\rho)$, the assumed constant wetting contact angle and triple contact line of EPS particle while residing on the deformed interface, and the assumed magnetic susceptibility of the EPS particles. The estimated and observed energy minima for the holmium-based paramagnetic liquid can be found in Figure S4, where the rationale for the difference between the theoretical estimation and experimental observations is almost the same as in the case of the manganese dichloride-based paramagnetic liquid.

The plots in Figure 4a-d show a local minimum or maximum at the centerline of the magnet ($\rho = 0$) from the meniscus energy E_I . This behavior is the result of a numerical error raised in calculating the second derivative of the interface deformation $u''(\rho)$ at the boundary. Physically, the E_I should have a monotonical increasing/decreasing progression at $\rho = 0$ instead of an abrupt change.

We note that previous studies of magnetophoresis (17, 18) discussed the force resulting from the magnetic energy, $F_M = -\nabla E_M$, which describes particle motion in the absence of capillary forces and weight and which cannot result in an off-center trapped state. We have replicated the experimental setup of the report (17) as depicted in Figure S1b, using the same type of magnetic liquid, i.e. manganese dichloride-based solution, but different particles. We also conducted experiments with holmium-based paramagnetic liquid. The pulling motion and off-center trapping at the base of the interface deformation on both paramagnetic liquids was observed for EPS particles (Figure S5-b and c).

Application of the trapping phenomena of particles on the air-paramagnetic liquid interface.

To demonstrate the potential application of the pulling motion and trapping mechanism, we performed directed particle self-assembly as shown in Figure 5a and Video S6. Four EPS particles, 1.5 to 2 mm in diameter, were initially residing on the air-manganese dichloride paramagnetic liquid interface (Figure 5a-i). The initial vertical position of the magnet is greater than 20 mm to avoid disturbing the interface of the paramagnetic liquid. The magnet was brought into the vicinity of the paramagnetic liquid ($h_M \approx 3 \text{ mm}$) and consequently caused the interface to deform. The closest particle to the magnet moved first towards the ring-shape potential well and remain being trapped. Then the rest of the particles also moved towards the trapping ring and eventually self-assembled to a line-like bundle. When the magnet was removed, the particles rearranged themselves forming

a T-like structure (Figure 5a-iii). The directed self-assembly was also demonstrated for EPS particles floating on top of a holmium-based paramagnetic liquid (Video S6).

We have also performed a robotic particle guiding of an EPS particle on the air-manganese dichloride paramagnetic liquid interface (Figure 5b). Figure 5b-i shows the top-view of the trajectories of the magnet and the EPS particle denoted with green and white color, respectively. The red star on the trajectory of the particle denotes the start position and the black star denotes the end position. The start and the end position of the magnet are overlapped. The X coordinates of the trajectories of the magnet and the particle are shown in Figure 5b-ii and the Y coordinates in Figure 5b-iii. The experiment started by bringing the magnet to the vicinity of the paramagnetic liquid at ~6-th second (full black vertical line from the left). The magnetic field from the magnet consequently instigated interface deformation. The EPS particle was attracted to the base of the interface deformation. The guiding was initiated at ~43-th second (black dashed vertical line from the left in Figure 5b ii and iii) and ended at ~203-th second (black dashed vertical line from the right). During this period, the magnet executed a square trajectory with a side of 20 mm at a speed of 0.5 mm/s. The magnet was retracted at ~210-th second (a full black line from the right). The correlation coefficients between the X and Y coordinates of the particle and the X and Y coordinates of the magnet were 0.907 and 0.918, respectively. The same experiment was also carried out for an EPS particle floating on air-holmium-based paramagnetic liquid (Video S7).

Summary

In summary, we have shown for the first time the pulling motion and trapping of solid spheroid particles on air-paramagnetic liquid interface induced by a magnet, and theoretically explained the underlying physical mechanism. The motion of a particle on the air-paramagnetic liquid interface can be treated as an energy minimization problem, which is a result of an interplay among the curvature of the deformed interface created by the non-uniform magnetic field as well as the effective mass and magnetic moment of the particle. The off-center trapping location of the EPS particles varies with the vertical position of the magnet with respect to the paramagnetic liquid. A closer distance between the magnet and the paramagnetic liquid results in a closer trapping location to the centerline of the magnet. A longer magnet-to-paramagnetic liquid distance results in a more distant trapping location from the centerline of the magnet. The theorized physical mechanism is compared to experiments. Potential applications in directed self-assembly and robotic particle guiding have also been demonstrated.

Materials and Methods

Experimental setup

An in-house developed 3D Cartesian positioning system (X, Y, Z) was constructed for experimental studies, as shown in Figure S1a. Two translational stages (M414.3PD, Physik Instrumente (PI), GmbH, Germany) were mounted on top of each other in a cross configuration for planar XY positioning. One translational stage (M404.8PD, Physik Instrumente (PI), GmbH, Germany) was mounted on top of the upper planar stage for vertical motion. The control of the positioning stages was realized by a control unit (C-884, Physik Instrumente (PI), GmbH, Germany). The execution of programmed movements was performed using in-house developed automation platform AutomationBase. A gamepad console (F710, Logitech, USA) was used for human-machine interaction.

Two custom-made aluminum fixtures were manufactured and assembled together in order to fit a $\phi 5$ mm hex key. A 25 mm \times $\phi 5$ mm NdFeB N45 magnet (supermagnete.de, Webcraft GmbH, German), attached to the bottom of the hex key was used for all of the experiments except for the replicated setup of reference (17). For the replicated setup as of reference (17) (Figure S1b), we employed a soft iron piece ($\phi \sim 2$ mm) and a 4 mm \times $\phi 36$ mm NdFeB magnet placed under the container filled with a paramagnetic liquid.

Petri dish caps (diameter: ~ 35 mm, height: ~ 5 mm and diameter: ~ 59 mm, height: ~ 7 mm) served as containers for paramagnetic liquids. The container with the paramagnetic liquid was placed on

a separate table from the 3D positioning system to reduce the influences from the mechanical vibration during the motion of the stages.

Images and videos were acquired using three Digital Single-Lens Reflex (DSLR) cameras (EOS 80D, Canon, Japan) with lens (EF 100, Canon, Japan). One camera was vertically mounted for top-view and the other two cameras were installed on tripods for side and bird's view.

Preparation of holmium-based and manganese dichloride paramagnetic liquids

Two types of paramagnetic salts were used, a holmium (iii) nitrate pentahydrate and a manganese dichloride. The concentration for the holmium based paramagnetic liquid was 2.27 mol/kg and 7.94 mol/kg for the manganese dichloride paramagnetic liquid. The paramagnetic salts were mixed within Milli-Q water.

Characterization of the magnetic moment of the paramagnetic liquids and particles

For both paramagnetic liquids as well as for the particles, the magnetization was measured for a sample size of 7 μl in a multipurpose measurement system (PPMS Dynacool, Quantum Design, USA) using Vibrating Sample Magnetometer (VSM) mode with an outer excitation magnetic field of ± 1 T with equally distributed step size. The volume magnetization curves of the paramagnetic liquids and the particles are shown in Figure S7.

Characterization of the density of the paramagnetic liquids

The mass of 0.5 ml Hamilton Syringe (Hamilton Company, Switzerland) was measured with a precision weight scale (Mettler Toledo, USA) and then the syringe was filled with paramagnetic liquid. The mass of the syringe filled with magnetic liquid was measured again with the precision weight scale. The difference was used to compute the density of the magnetic liquid. The densities of the magnetic liquids are reported in Table S1.

Characterization of the surface tension of the paramagnetic liquids

The surface tension of the paramagnetic liquids was measured using a tensiometer (Attension® Theta, Biolin Scientific, Sweden). The values of the surface tension are reported in Table S1.

Characterization of the viscosity of the paramagnetic liquids

The viscosity of the paramagnetic liquids was measured using a rheometer (Physica MCR 302, Anton Paar GmbH, Austria). Approximately 1ml of magnetic liquid was inserted between the stationary plate and the rotating probe CP 50-1 with a gap of 1 mm. The viscosity measurement protocol was adapted from (26) and slightly modified. Initially, the temperature was set to 23°C and was kept constant throughout all steps. Before recording the data, the paramagnetic liquid was stirred at a constant shear rate of 100 s^{-1} for 30 seconds. Then the shear rate was varied from 1 to 800 s^{-1} with 30 assigned values distributed logarithmically, each lasting for 30 seconds. The response of a paramagnetic liquid was measured every 30 seconds before the shear rate is being altered to a new value. The viscosities of the paramagnetic liquids are reported in Table S1.

Characterization of the contact angles of the particles when floating to the paramagnetic liquids

The measurements were carried out using the previously mentioned in-house developed experimental setup. In this case, only the side view camera was used. Static contact angle measurements were performed. Three particles from the same type were placed on top of a paramagnetic liquid and a video was taken. The most preferred frame was extracted from the video later in MATLAB (MathWorks, USA). Each frame was further analyzed. A suitable Region of Interest (ROI) with a particle on top of a paramagnetic liquid was identified, followed by histogram adjustment and edge detection using the Canny algorithm (27). The identified edges were overlaid to the original ROI and the contact angle was measured by a triangular screen ruler (MB tool, Germany). From each image, two measurements were realized for each of the three particles of the same type, resulting in six measurements per particle type. The values were averaged to acquire the mean contact angle and the standard deviation was also computed. The contact angle

of the particles with the paramagnetic liquids are reported in Table S3. Part of the procedure for experimental identification of the contact angle is illustrated in Figure S6.

Characterization of the magnetic field of the $\phi 5 \times 25 \text{ mm}^2$ NdFeB N45 magnet

The magnet was installed on the 3D positioning system and brought into contact with the probe of a magnetometer (Gaussmeter Model 410, Lake Shore Cryotronics, Inc, USA). Then the magnet was retracted away from the probe with steps of $100 \mu\text{m}$ for a range of 20 mm. The readings from the magnetometer were recorded. The experiment was repeated three times and the average of three readings was computed. The magnetic field gradient was numerically computed in MATLAB (MathWorks, USA). The magnetic field and field gradient of the magnet are shown in Figure S7.

Preparation procedure prior to the experiments

Before the experiments, the air-paramagnetic liquid interface was firstly adjusted as flat as possible by filling magnetic liquid into the container until a convex interface was observed and then liquid was removed using a syringe until the interface became flat to diminish the wall effects.

Note on the utilized particles

PS and PE particles obtained from the supplier (Cospheric LLC, USA) are spherical with a maximum 10% size variation. The EPS particles also featured minor shape variations, but they dominantly resembled spherical shape. The hollow ceramic particles (Extendspheres® 200/600, SphereOne™) have large shape variations, the most spheroid particles were manually extracted from a population of hundreds of particles under an optical microscope.

Characterization of a varying interface deformation of a paramagnetic liquid

A $\sim 59 \text{ mm}$ container was filled with a paramagnetic liquid and an EPS particle was placed on the air-paramagnetic liquid interface. The $25 \text{ mm} \times \phi 5 \text{ mm}$ magnet was brought as close to the air-paramagnetic liquid interface to induce an interface deformation until the paramagnetic liquid was about to engulf the magnet. Then the magnet was retracted away from the paramagnetic liquid with a step size of $100 \mu\text{m}$ for 1 mm and then the magnet was brought back in the same manner until the interface was again fully deformed. Eventually, the magnet was retracted. While deforming the interface at different magnet-to-paramagnetic liquid distances, an EPS particle would change its position with respect to the centerline of the magnet. When the magnet was in its initial or terminal position ($> 10 \text{ mm}$), i.e. far away from the paramagnetic liquid, the EPS particle was used to identify the base line, i.e. the undisturbed air-paramagnetic liquid interface. Video S4 shows the experimental profiling of the interface deformation and its influence on the trapping position of an EPS particle. The datapoints for the maximum interface deformation h_L was obtained by analyzing the video from the side view, whereas the data for the trapping location of an EPS particle δ_{EPS} was obtained from the top view video.

During the experiments, when the magnet surpassed a certain closeness to the paramagnetic liquid (small h_M), the paramagnetic liquid engulfed the magnet and a liquid bridge was formed. The engulfing is not shown on the plots in Figure 2b and c and this undesired scenario was not subject of this study.

Numerical Simulations

Comsol Multiphysics 5.3a (Comsol Group, Sweden) was used for simulation of the magnetic field, field gradients and magnetic tensor exerted on a magnetic liquid from a NdFeB permanent magnet. A 2D axisymmetric model was constructed with the geometry of the real system. Custom-defined materials were used to specify the properties of the magnet and the magnetic liquids. The magnetization of the paramagnetic liquids was defined through the experimentally obtained relative permeability. A stationary magnetic field study was used to generate the magnetic fields and field gradients. The vertical component B_z , the radial component B_ρ and the norm $|B|$ of the magnetic flux density along with the norm component of the magnetic field $|H|$ were exported to MATLAB (MathWorks, USA).

The interface deformations were computed using the double integral given in Equation (8) in MATLAB (MathWorks, USA). The interface deformation was smoothed with MATLAB's smooth function and later within curve-fitting application utilizing Smoothing Spline (with R2 greater than 99 %). The first derivative of the deformation was numerically computed. The same smoothing procedure was applied followed by the computation of the second derivative. After obtaining the first and the second derivatives of the meniscus deformation, the mean curvature, Equation (S26) was computed. Finally, the energy profiles of the gravitational, the capillary and the magnetic energies were computed in order to analyze the differences in their influence. The total energy was obtained by summing these contributions and the adsorption energy (Equations 1 or 7). In case of the EPS particles, the total energies were also smoothed utilizing the MATLAB's function Smoothing Spline. The smoothing has been performed reduce the impact from the numerical error in the second derivative of the interface deformation u'' and consequently to obtain the total energy minimum, i.e. the trapping location.

Analysis of the trajectories of the particle and the magnet

The experimental video data was imported into MATLAB (MathWorks, USA) and analyzed using a tailor-made script. The position of the particle is detected using the Circular Hough Transform (28). The magnet was traced using a template-matching based algorithm. The trajectories of both the particle and the magnetic were computed based on the particle/magnet position at each frame. Missing data was a result of occlusion of the particle by the magnet or failure of the template-matching algorithm from the sudden change in intensity of the scene.

Additional details can be found in the Supporting Information, which includes a note to the Supporting Videos, the complete theoretical derivation of the interface deformation and the energy potentials; as well as Supporting Figures and Tables.

Acknowledgments

This research work was supported by the Academy of Finland (projects #304843 and #296250) and the Aalto University ASci/ELEC Thematic Research Programme. ZC thanks the Neles Foundation for the incentive stipend. All authors would like also to express their gratitude to Seppo Nurmi for insightful feedback on the design and manufacturing of the mechanical parts, to Mika Latikka for experimental measurements of the magnetic properties of the paramagnetic liquids and particles as well as for lending the flat cylindrical magnet; to research scientist Dr. Michael Hummel, Dr. Meri Lundahl, Ph.D. candidates Gabriela Berto and Risto Koivunen for helping in performing viscosity measurements, to SphereOne Inc. for the provision of the hollow ceramic (HC) particles - Extendspheres® 200/600, to Professor Jaakko Timonen for fruitful discussion, feedback, and contributions to the Comsol modeling, as well as to Professor Veikko Sariola for pre-reviewing this manuscript.

Note: The PhD thesis of Zoran Cenev (29) contains an earlier version of this manuscript.

References

1. D. L. Hu, B. Chan, J. W. M. Bush, The hydrodynamics of water strider locomotion. *Nature* **424**, 663–666 (2003).
2. D. L. Hu, J. W. M. Bush, Meniscus-climbing insects. *Nature* **437**, 733–736 (2005).
3. W. Hu, G. Z. Lum, M. Mastrangeli, M. Sitti, Small-scale soft-bodied robot with multimodal locomotion. *Nature* **554**, 81–85 (2018).
4. A. Diguët, *et al.*, Photomanipulation of a droplet by the chromocapillary effect. *Angew. Chemie - Int. Ed.* **48**, 9281–9284 (2009).

5. N. Kavokine, *et al.*, Light-Driven Transport of a Liquid Marble with and against Surface Flows. *Angew. Chemie - Int. Ed.* **55**, 11183–11187 (2016).
6. G. Lumay, N. Obara, F. Weyer, N. Vandewalle, Self-assembled magnetocapillary swimmers. *Soft Matter* **9**, 2420–2425 (2013).
7. G. Grosjean, *et al.*, Remote control of self-assembled microswimmers. *Nat. Publ. Gr.*, 1–8 (2015).
8. A. Snezhko, I. S. Aranson, W. K. Kwok, Surface wave assisted self-assembly of multidomain magnetic structures. *Phys. Rev. Lett.* **96**, 1–4 (2006).
9. A. Snezhko, I. S. Aranson, Magnetic manipulation of self-assembled colloidal asters. *Nat. Mater.* **10**, 698–703 (2011).
10. M. Cavallaro, L. Botto, E. P. Lewandowski, M. Wang, K. J. Stebe, Curvature-driven capillary migration and assembly of rod-like particles. *Proc. Natl. Acad. Sci.* **108**, 20923–20928 (2011).
11. T. V. Vinay, T. N. Banuprasad, S. D. George, S. Varghese, S. N. Varanakkottu, Additive-Free Tunable Transport and Assembly of Floating Objects at Water-Air Interface Using Bubble-Mediated Capillary Forces. *Adv. Mater. Interfaces* **4**, 1601231 (2017).
12. L. Foret, A. Würger, Electric-Field Induced Capillary Interaction of Charged Particles at a Polar Interface. *Phys. Rev. Lett.* **92**, 4 (2004).
13. M. Frenkel, *et al.*, Toward an Understanding of Magnetic Displacement of Floating Diamagnetic Bodies, I: Experimental Findings. *Langmuir* **34**, 6388–6395 (2018).
14. I. Legchenkova, *et al.*, Magnetically inspired deformation of the liquid/vapor interface drives soap bubbles. *Surf. Innov.* **6**, 231–236 (2018).
15. O. Gendelman, *et al.*, Study of the Displacement of Floating Diamagnetic Bodies by Magnetic Field. *Surf. Innov.*, 1–8 (2019).
16. E. Bormashenko, Moses effect: physics and applications. *Adv. Colloid Interface Sci.* **269**, 1–6 (2019).
17. B. A. Grzybowski, Static and Dynamic Self-Organization. *PhD Thesis* (2000).
18. J. V. I. Timonen, B. A. Grzybowski, Tweezing of Magnetic and Non-Magnetic Objects with Magnetic Fields. *Adv. Mater.* **29**, 1603516 (2017).
19. Y. Gao, Y. C. Jian, L. F. Zhang, J. P. Huang, Magnetophoresis of nonmagnetic particles in ferrofluids. *J. Phys. Chem. C* **111**, 10785–10791 (2007).
20. J. Vialetto, *et al.*, Magnetic Actuation of Drops and Liquid Marbles Using a Deformable Paramagnetic Liquid Substrate. *Angew. Chemie Int. Ed.* **56**, 16565–16570 (2017).
21. N. Hirota, *et al.*, Rise and fall of surface level of water solutions under high magnetic field. *Jpn. J. Appl. Phys.* **34**, L991–L993 (1995).
22. D. Y. C. Chan, J. D. Henry, L. R. White, The interaction of colloidal particles collected at fluid interfaces. *J. Colloid Interface Sci.* **79**, 410–418 (1981).
23. P. A. Kralchevsky, K. Nagayama, Capillary forces between colloidal particles. *Langmuir* **10**,

23–36 (1994).

24. J. Léandri, A. Würger, Trapping energy of a spherical particle on a curved liquid interface. *J. Colloid Interface Sci.* **405**, 249–255 (2013).
25. M. Hayakawa, *et al.*, Effect of moderate magnetic fields on the surface tension of aqueous liquids: A reliable assessment. *RSC Adv.* **9**, 10030–10033 (2019).
26. K. Shah, S.-B. Choi, The Field-Dependent Rheological Properties of Magnetorheological Fluids Featuring Plate-Like Iron Particles. *Front. Mater.* **1**, 1–6 (2014).
27. J. Canny, A Computational Approach to Edge Detection. *IEEE Trans. Pattern Anal. Mach. Intell.* **PAMI-8**, 679–698 (1986).
28. T. J. Atherton, D. J. Kerbyson, Size invariant circle detection. *Image Vis. Comput.* **17**, 795–803 (1999).
29. Z. Cenev, “Particle Micromanipulation Using Single Magnetic Sources,” Aalto University. (2019).

Figures and Tables

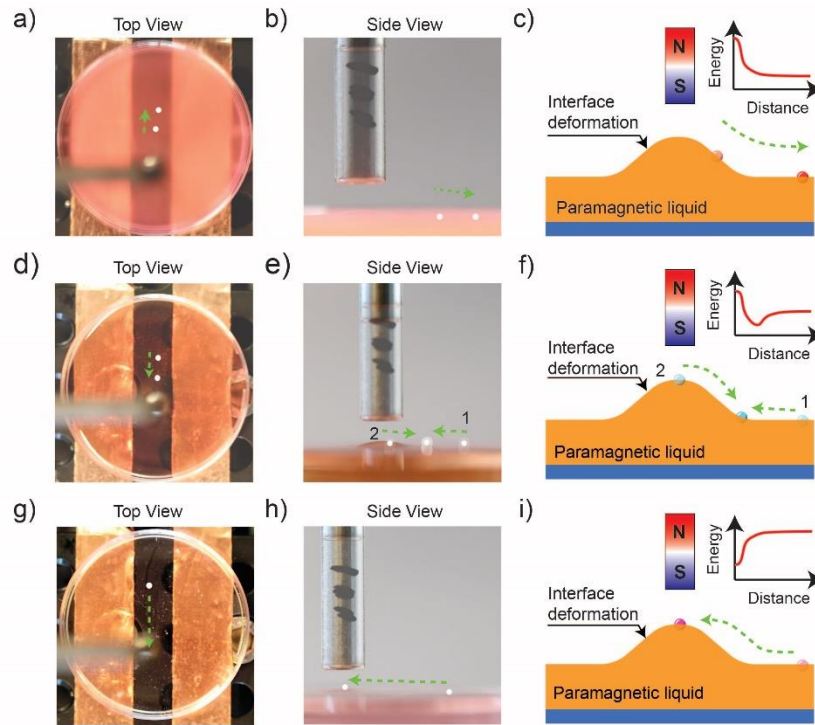


Figure 1. Different motion modes of spheroid particles on air-paramagnetic liquid interface observed experimentally (a-b, d-e, g-h) and corresponding illustrations (c, f, i). Illustrations not to scale. Particle visibility in (a-b, d-e, g-h) graphically enhanced with white dots. Green arrows denote the direction of particle motion. **a-c)** A PE spherical particle on the air-paramagnetic liquid interface is pushed away from the magnet. The paramagnetic liquid is holmium-based. **d-f)** An EPS particle on the air-liquid interface of holmium-based paramagnetic liquid. The particle is pulled (1) or pushed (2) and finally trapped at the base of the interface deformation created by the magnet. **g-i)** Magnetic spheroid HC particle on the air-liquid interface of manganese dichloride-based paramagnetic liquid is trapped at the peak of the meniscus. a), d) g) illustrate the top views and b), e), h) the side views. a), b), h) are superimposed images of before and after meniscus formation; d) shows the initial position (1) and the trapping location of the particle; g) shows only the initial position of the particle; e) is an image consisting of three superimposed images, two images of starting positions (1 and 2) and one image of the final trapping location. Schematic energy profiles of the particles are shown as insets in c), f) and i) where the vertical axis corresponds to the centerline of the magnet.

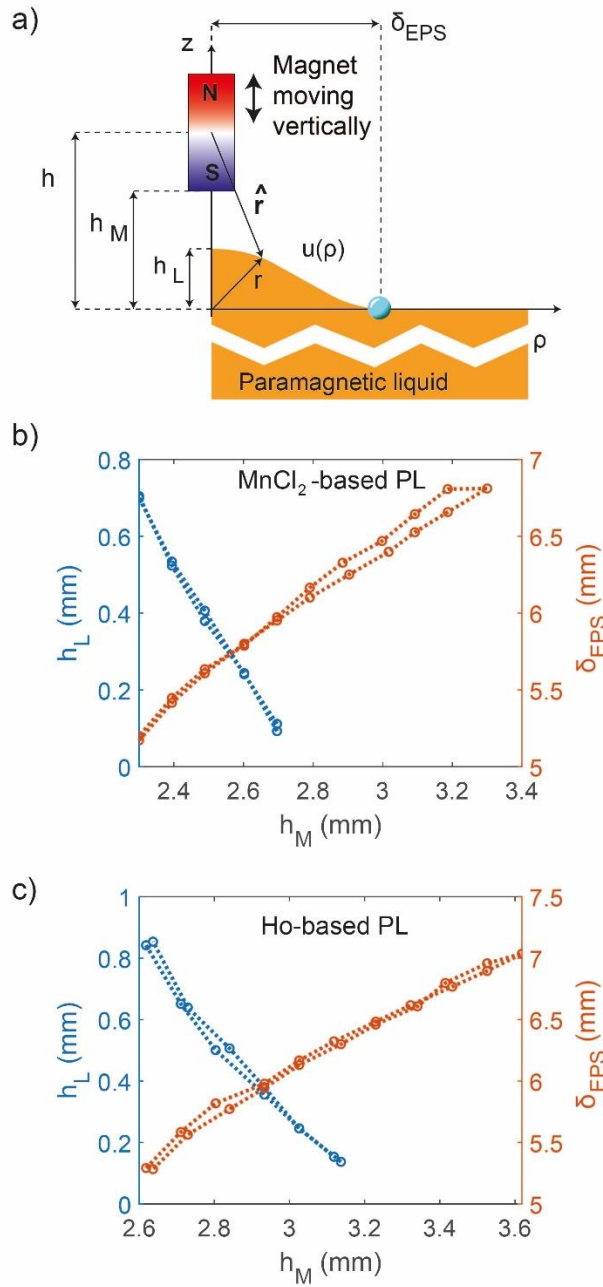


Figure 2. Definition of parameters and effects of air-paramagnetic liquid interface deformation. **a)** System configuration including a magnet and a deformed interface. Illustration not to scale. The vector \vec{r} is defined with respect to the origin in the plane of the flat interface, whereas \hat{r} is defined with respect to the center of the magnet. Accordingly, $r = \sqrt{\rho^2 + z^2}$ and $\hat{r} = \sqrt{\rho^2 + (z - h)^2}$. The meniscus deformation $u(\rho)$ has its maximum value at the center, thus yielding the maximum interface deformation h_L . The magnet position is denoted with h_M . δ_{EPS} denotes the trapping location of an EPS particle with respect to the centerline of the magnet. **b and c)** Experimental results on the h_L and δ_{EPS} as a function of h_M for **b)** manganese dichloride-based paramagnetic liquid and **c)** holmium-based paramagnetic liquid.

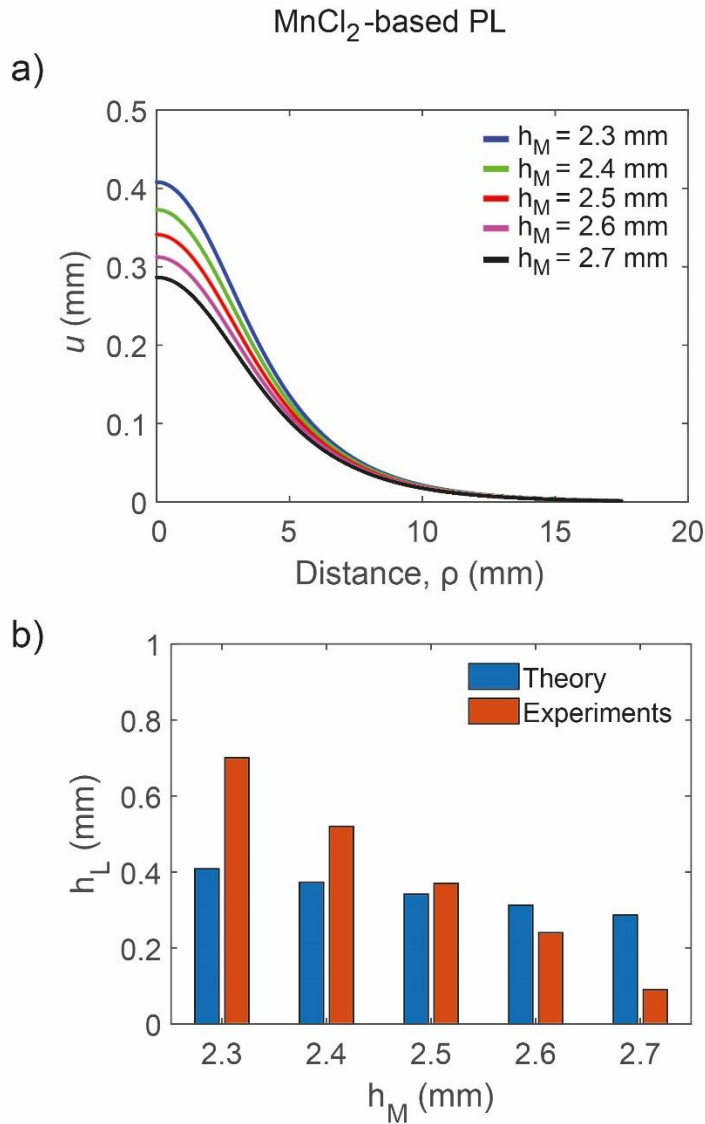


Figure 3. A theoretical model for deformed interface and comparison to experimental results for manganese dichloride-based paramagnetic liquid. **a)** Numerical simulation of the Interface deformation $u(\rho)$ for five different vertical positions of the magnet, i.e. 2.3, 2.4, 2.5, 2.6 and 2.7. **b)** The theoretical prediction compared with the experimental measurement of the maximum interface deformation h_L for at five different vertical positions of the magnet.

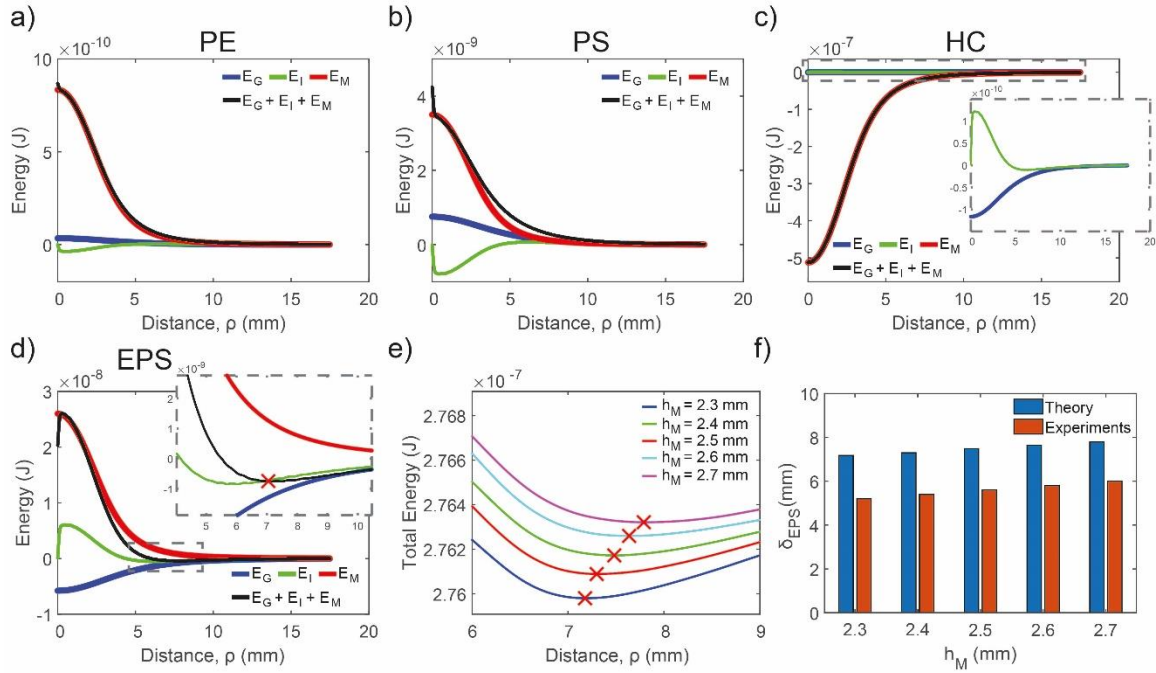


Figure 4. Numerical estimation of energy profiles and comparisons to experimental measurements for manganese dichloride-based paramagnetic liquid. Individual energy contributions for **a)** a PE particle **b)** a PS particle **c)** an HC particle and **d)** a 1.5 mm EPS particle. The numerical simulations consider a magnet position of 2.3 mm in (a-c) and 2.6 mm in d). **e)** Numerically estimated total energy minimum, i.e. trapping location of an EPS particle at 5 different magnet positions h_M . **f)** The theoretical estimation **e)** compared with the experimental measurement of a trapping location of an EPS particle δ_{EPS} at five different vertical positions of the magnet. The insets in gray dashed boxes in c) and d) are magnified views for the close-in plots. The red "x" signs in d) and e) denote energy minima.

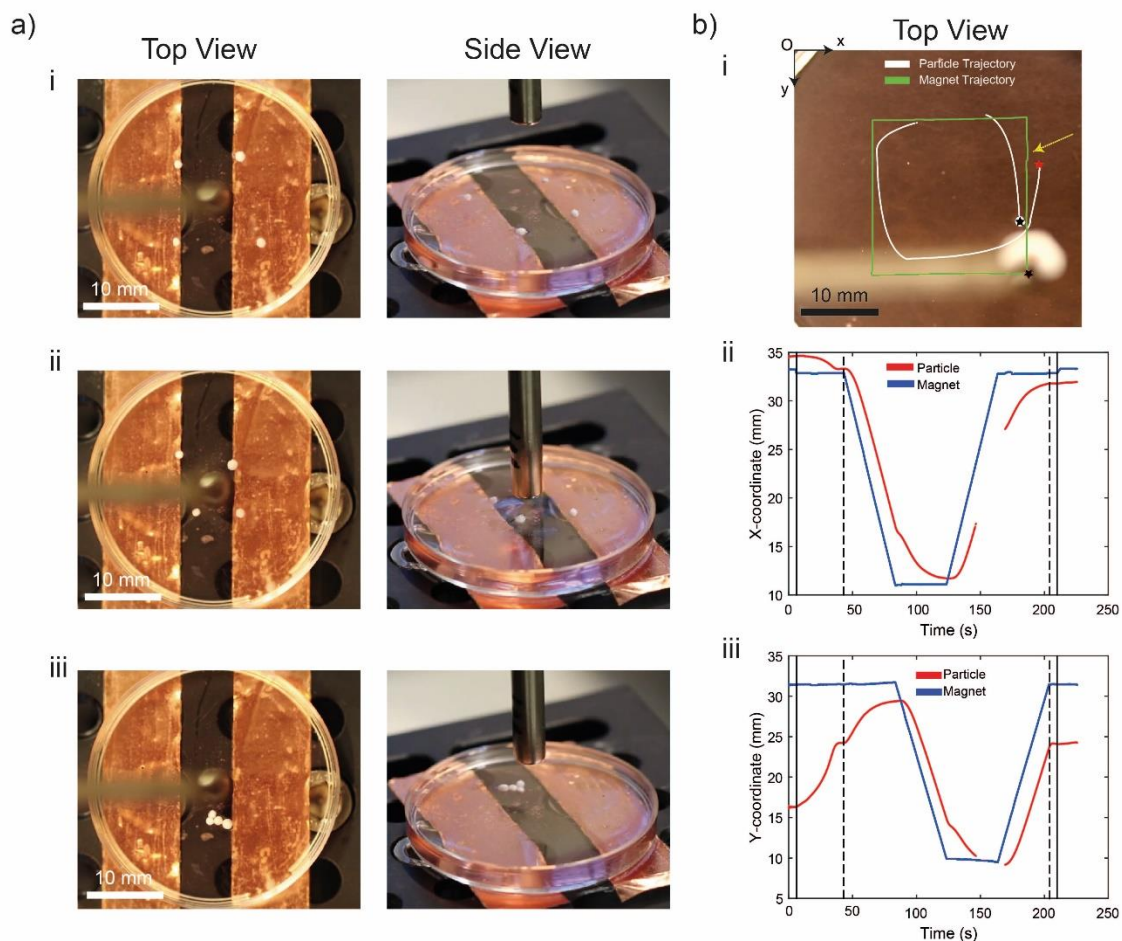


Figure 5. Application cases of the pulling motion and trapping of the EPS particles on the air-paramagnetic liquid interface. **a)** Directed self-assembly of four EPS particles (Video S6): i) four EPS particles residing on the air-manganese dichloride-based paramagnetic liquid interface. The magnet is perpendicular to the interface at a distance greater than 20 mm; ii) The magnet approaches the liquid surface and forms an interface deformation which in turn pulled the particles into the trapping ring; iii) The particles self-assembled into a line formation and after the magnet was removed the particles rearranged to a triangle-like formation. **b)** Robotic particle guiding (Video S7): i) Robotic guiding of EPS particle on the air-manganese dichloride-based paramagnetic liquid interface. The trajectories of the magnet and the particle are shown in white and green, respectively. Red stars denote start positions and black stars denote end positions. The yellow arrow shows a local error of the magnet tracking algorithm. ii) X-coordinate of the trajectories for the particle (red) and the magnet (blue); iii) Y-coordinate of the trajectories for the particle (red) and the magnet (blue). For ii) and iii) the curves have missing data due to occlusion of the particle by the magnet or inadequate images for processing.